Monthly Notices
of the
ROYAL ASTRONOMICAL SOCIETY

MNRAS **428,** 2311–2320 (2013) doi:10.1093/mnras/sts195

The simulation of molecular clouds formation in the Milky Way

S. A. Khoperskov,[1]⋆ E. O. Vasiliev,[2] A. M. Sobolev[3] and A. V. Khoperskov[4]

[1]*Institute of Astronomy Russian Academy of Sciences, Pyatnitskaya st. 48, 119017 Moscow, Russia*
[2]*Institute of Physics, Department of Physics, Southern Federal University, Stachki Ave. 194, 344090 Rostov-on-Don, Russia*
[3]*Ural Federal University, Lenin ave. 51, 620000 Ekaterinburg, Russia*
[4]*Volgograd State University, Universitetskiy pr. 100, 400062 Volgograd, Russia*

Accepted 2012 October 11. Received 2012 October 6; in original form 2012 July 24

ABSTRACT

Using 3D hydrodynamic calculations we simulate formation of molecular clouds in the Galaxy. The simulations take into account molecular hydrogen chemical kinetics, cooling and heating processes. Comprehensive gravitational potential accounts for contributions from the stellar bulge, two- and four-armed spiral structure, stellar disc, dark halo and takes into account self-gravitation of the gaseous component. Gas clouds in our model form in the spiral arms due to shear and wiggle instabilities and turn into molecular clouds after $t \gtrsim 100$ Myr. At the times $t \sim 100$–300 Myr the clouds form hierarchical structures and agglomerations with the sizes of 100 pc and greater. We analyse physical properties of the simulated clouds and find that synthetic statistical distributions like mass spectrum, 'mass–size' relation and velocity dispersion are close to those observed in the Galaxy. The synthetic l–v (galactic longitude–radial velocity) diagram of the simulated molecular gas distribution resembles observed one and displays a structure with appearance similar to molecular ring of the Galaxy. Existence of this structure in our modelling can be explained by superposition of emission from the galactic bar and the spiral arms at ∼3–4 kpc.

Key words: ISM: clouds – Galaxy: structure – galaxies: ISM.

1 INTRODUCTION

Molecular clouds represent one of the major constituents of our galaxy (Dame, Hartmann & Thaddeus 2001). Their masses and sizes vary in a wide range (e.g. Solomon et al. 1987). Molecular clouds play very important role in determination of the structure and evolution of the Galaxy. This can be illustrated by the fact that the stars and their clusters originate from molecular clouds (Shu, Adams & Lizano 1987; Lada & Lada 2003; McKee & Ostriker 2007). The dynamical time of disintegration for molecular clouds in the Milky Way is much shorter than the rotation period of the galaxy (e.g. Blitz & Shu 1980). So, explanation of the observational fact of existence of the rich population of molecular clouds requires involvement of efficient mechanisms leading to formation of molecular clouds in the Galaxy. Special interest is paid to formation of the giant molecular clouds (GMCs) which have masses $\gtrsim 10^6$ M$_\odot$ (Dame et al. 1986). Two main theories of the GMCs formation were proposed. The first one explains formation of the GMCs by large-scale magnetic and/or gravitational instabilities (Elmegreen 1979, 1994; Balbus & Cowie 1985; Chou et al. 2000; Kim & Ostriker 2006). In the second one the GMCs are built up by coalescence of the smaller molecular clouds (Field & Saslaw 1965; Levinson & Roberts 1981; Tomisaka 1984; Kwan & Valdes 1987; Roberts & Stewart 1987) or interaction of the turbulent flows (e.g. Ballesteros-Paredes et al. 2007). In reality both types of processes are expected to play significant role (Zhang & Song 1999; Dobbs 2008).

Large-scale perturbations in a gas of the Galactic disc can be generated not only by magnetic fields or self-gravity but also by the galactic spiral shock wave (Roberts 1969; Nelson & Matsuda 1977). A simple analysis of the global galactic shock wave shows that such shocks are unstable (Mishurov & Suchkov 1975). Obviously, large-scale shear flows in the Galactic shocks lead to the development of both wiggle and Kelvin–Helmholz instabilities (Wada 2001; Wada & Koda 2004). Such hydrodynamic instabilities are expected to give a birth to spurs, gaseous fragments and turbulent flows (Wada 1994; Wada, Spaans & Kim 2000; Dobbs & Bonnel 2006; Shetty & Ostriker 2006; Khoperskov et al. 2011). The gravitational and thermal (in general, thermochemical) instabilities are expected to develop further fragmentation that leads to formation of the population of molecular clouds.

The properties of molecular clouds (mass, size, density, temperature etc.) are intensively studied both observationally (Solomon et al. 1987; Falgarone, Puget & Perault 1992; Lada et al. 2008; Heyer et al. 2009; Rathborne et al. 2009; Kauffmann et al. 2010; Román-Zúñiga et al. 2010) and numerically (Dobbs, Bonnell & Pringle 2006; Dobbs & Bonnell 2007a,b; Tasker & Tan 2009; Glover & Mac Low 2011). Efforts in order to understand

⋆ E-mail: khoperskov@inasan.ru

dependencies between physical parameters of the clouds lead to establishment of several empirical relationships for the properties of molecular clouds (Larson 1981). In particular, the mass–size relation reflects the hierarchical spatial structure of clouds (Beaumont et al. 2012). Molecular clouds can agglomerate in small groups and chains, thus reflecting processes of the cloud formation: disintegration into smaller clumps or combining into bigger clouds. Because of the origin of the clouds from the large-scale perturbations in the galactic disc molecular clouds can trace the large-scale structures, e.g. spiral arms and the bar (e.g. Wada & Koda 2004). Several observational studies display existence of the galactic molecular ring (Stecker et al. 1975; Cohen & Thaddeus 1977; Román-Duval et al. 2010), however, it is unclear whether this is an actual ring or just superposition of emission from molecular clouds belonging to different spiral arms (Dobbs & Burkert 2012).

In this paper we develop a model aiming to reproduce general characteristics of the formation of molecular clouds in the Galaxy, their physical properties, their distribution in the Milky Way using the 3D simulations with the comprehensive gravitational potential, self-gravity of gaseous component, molecular hydrogen chemical kinetics and cooling and heating processes.

The paper is organized as follows. Section 2 describes basic premises and equations of our model. Section 3 presents numerical results on the disc evolution. Section 4 presents analysis of the physical properties of the clouds in our model. Section 5 considers large-scale structures in the simulated Galaxy. Section 6 summarizes the results.

2 MODEL

2.1 Gas dynamics and galaxy potential

The dynamics of the chemically reacting gas mixture in our model of the Galaxy can be written in the single-fluid approximation as follows:

$$\frac{\partial \rho}{\partial t} + \nabla \cdot (\rho \boldsymbol{u}) = 0, \tag{1}$$

$$\frac{\partial \rho \chi_i}{\partial t} + \nabla \cdot (\rho \boldsymbol{u} \chi_i) = \rho s_i, \quad i = 1, \ldots, n_\mathrm{s}, \tag{2}$$

$$\frac{\partial \boldsymbol{u}}{\partial t} + \nabla \cdot (\boldsymbol{u} \otimes \boldsymbol{u}) = -\frac{\nabla p}{\rho} - \nabla(\Psi_\mathrm{ext} + \Psi_\mathrm{g}), \tag{3}$$

$$\frac{\partial E}{\partial t} + \nabla \cdot ((E + p) \cdot \boldsymbol{u}) = -\boldsymbol{u} \cdot \nabla(\Psi_\mathrm{ext} + \Psi_\mathrm{g}) - (\Lambda - \Gamma), \tag{4}$$

where ρ is the gas density, p is the gas pressure, $\boldsymbol{u} = (u, v, w)$ is the gas velocity vector, n_s is the number of components in the gas mixture (in our model $n_\mathrm{s} = 2$), $\chi_i = \rho_i/\rho$ is the mass fraction of ith component of gas, $\sum_{i=1}^{n_\mathrm{s}} \chi_i = 1$, s_i is the formation/destruction rate of ith component, $E = \rho(e + \frac{u^2}{2})$ is the total energy, e is the specific internal energy, Λ and Γ are the cooling and heating rates, respectively, Ψ_g is the gravitational potential of gas, Ψ_ext is the total external gravitational potential produced by the massive dark halo Ψ_halo, the stellar bulge Ψ_bulge and the stellar disc Ψ_disc. The latter includes the potentials of the spiral structure and the bar. The potential of the gaseous component is determined by the Poisson equation:

$$\Delta \Psi_\mathrm{g} = 4\pi G \rho. \tag{5}$$

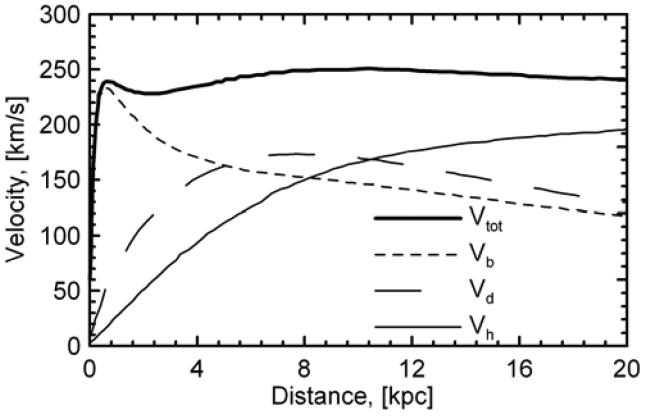

Figure 1. The rotation curve of the gas components in our model of the Galaxy, V_tot (thick solid line). The contributions from the stellar bulge, V_b, the stellar disc, V_d, and the dark halo, $V_\mathrm{h}(r)$, are shown by dash, long dash and thin solid lines, respectively.

The external gravitational potential can be written as follows:

$$\Psi_\mathrm{ext} = \Psi_\mathrm{halo} + \Psi_\mathrm{bulge} + \Psi_\mathrm{disc}. \tag{6}$$

In our model we imposed a large-scale gravitation potential of Milky Way spiral structure. Recent observational data show that the Milky Way spiral structure is well described by the four-arm model (Vallee 2005; Levine, Blitz & Heiles 2006). A detailed spiral structure decomposition was made by Lepine, Mishurov & Dedikov (2001), who had found that the Milky Way spiral structure is better described by superposition of $m = 2$ and $m = 4$ spirals modes which, in general, corresponds to the four-arm pattern. Hence, in our simulations we implement combination of two- and four-arm spiral potentials for the stellar disc. More detailed model of the gravitational potential is described in Appendix A.

Fig. 1 presents the rotation curve of the gas components adopted in our model of the Galaxy. For the maximum rotation velocity of the Milky Way we adopt a value obtained from the analysis of the recent observational data on the Galactic masers (Bobylev & Bajkova 2010). The external gravitational potential of the Galactic subsystems, e.g. stellar bulge, stellar disc and dark halo, Φ_ext, produces this rotation curve with the parameters for the Galactic subsystems fitted by Khoperskov & Tiurina (2003). The detailed description of the gravitational potential components is given in Appendix A.

In our calculations we use the value of the angular velocity of the spiral structure $\Omega_\mathrm{p} = 31\,\mathrm{km\,s^{-1}\,kpc^{-1}}$. This value is realized at the radius of corotation $R_\mathrm{c} \sim 8\,\mathrm{kpc}$ (Bobylev & Bajkova 2010). Our simulations have shown that variation of Ω_p in the range 18–28 $\mathrm{km\,s^{-1}\,kpc^{-1}}$ (Lepine et al. 2001; Amores, Lepine & Mishurov 2009; Sofue, Honma & Omodaka 2009) does not produce significant changes in the general properties of evolution of gas in the simulated Galaxy.

2.2 Chemical kinetics

H_2 molecules in the interstellar medium are formed on the surface of the dust grains and dissociated by ultraviolet Lyman–Werner photons and cosmic rays. We suppose that the dust density is proportional to the gas density because the dust is well mixed with gas on the scales of our simulations. Thus, evolution of molecular hydrogen number density can be found from (Bergin et al. 2004)

$$\frac{\mathrm{d}n_{\mathrm{H}_2}}{\mathrm{d}t} = R_\mathrm{gr}(T) n_\mathrm{H} n - [\zeta_\mathrm{H} + \zeta_\mathrm{diss}(N_{\mathrm{H}_2}, A_\mathrm{V})] n_{\mathrm{H}_2}, \tag{7}$$

where $n_{\rm H}$, $n_{\rm H_2}$ are the number densities of atomic and molecular hydrogen, respectively, $n = n_{\rm H} + 2n_{\rm H_2}$ is the total number density of hydrogen species, $N_{\rm H_2}$ is the H_2 column density, $R_{\rm gr}(T) = 2.2 \times 10^{-18} S T^{0.5}$ is the H_2 formation rate on dust grains (Tielens & Hollenbach 1985), $S = 0.3$ is the efficiency of the H_2 formation on dust (Cazaux & Tielens 2004), $\zeta_{\rm H} = 6 \times 10^{-18}$ s^{-1} is the cosmic ray ionization rate and $A_{\rm V}$ is the extinction. Following Draine & Bertoldi (1996) the photodissociation rate can be estimated as

$$\zeta_{\rm diss}(N({\rm H_2}), A_{\rm V}) = \zeta_{\rm diss}(0) f_{\rm shield}(N({\rm H_2})) f_{\rm dust}, \quad (8)$$

where $\zeta_{\rm diss}(0) = 4.17 \times 10^{-11}$ s^{-1} is the unshielded photodissociation rate, $f_{\rm shield}(N({\rm H_2}))$ is the H_2 self-shielding factor, $f_{\rm dust} = \exp(-\tau_{\rm d,\,1000})$ is the dust absorption factor (Draine & Bertoldi 1996) and $\tau_{\rm d,\,1000} = 10^{-21}(N({\rm H}) + 2N({\rm H_2}))$ is the optical depth due to dust grains at a wavelength $\lambda = 1000$ Å, which relates to the visual extinction as $\tau_{\rm d,\,1000} = 3.74 A_{\rm V}$.

To calculate the factors $f_{\rm shield}$ and $f_{\rm dust}$ we need to know both molecular, $N(H_2)$, and total, $N_{tot} = N({\rm HI}) + 2N({\rm H_2})$, hydrogen column densities. In order to do this accurately we should find a cumulative ultraviolet radiation field produced by the young stars and their clusters. Obviously, this problem is extremely complex, moreover, star formation processes are not included in our model. Hence, we follow a simplified approach introduced by Dobbs (2008). We use a simple estimate that the column densities of the chemical species are just the local densities of these species multiplied by the typical distance to a young star, $l_{\rm ph}$: $N({\rm H\,I,H_2}) = l_{\rm ph} n({\rm H\,I,H_2})$. This distance is assumed to be a constant length scale for the whole disc. In our simulations we take $l_{\rm ph} = 30$ pc, which is in agreement with the number of massive stars expected from the Salpeter initial mass function.

We assume that the Galactic gas has solar metallicity with the abundances given in Asplund, Grevesse & Sauval (2005): $[{\rm C/H}] = 2.45 \times 10^{-4}$, $[{\rm O/H}] = 4.57 \times 10^{-4}$ and $[{\rm Si/H}] = 3.24 \times 10^{-5}$. We assume that the dust depletion factors are equal to 0.72, 0.46 and 0.2 for C, O and Si, respectively. Chemical kinetics of the heavy elements is not solved in our model. We suppose that the carbon and silicon are singly ionized and oxygen stays neutral. This assumption is acceptable for the interstellar medium of the Milky Way due to existence of the strong ultraviolet radiation in the range ~10–13 eV (Habing 1968). The electron fraction is assumed to have constant value of 10^{-5} for all considered period of time. This level of ionization is assumed to be supported by the cosmic ray ionization rate assumed in our calculations. For $T \sim 10^4$ K the ionization fraction should obviously be higher, but the shock waves in our simulations are not strong enough to heat significant mass of gas to the temperatures this high, which is clearly seen at the phase diagram in the Section 3.

2.3 Cooling and heating processes

The cooling rates are computed separately for the temperatures below and above 2×10^4 K. In the low temperature range the cooling rate Λ in the energy equation (4) includes the typical processes of radiative losses for the interstellar medium (see details in Appendix B): cooling due to recombination and collisional excitation and free–free emission of hydrogen (Cen 1992), molecular hydrogen cooling (Galli & Palla 1998), cooling in the fine structure and metastable transitions of carbon, oxygen and silicon (Hollenbach & McKee 1989), energy transfer in collisions with the dust particles (Wolfire et al. 2003) and recombination cooling on the dust (Bakes & Tielens 1994). In the high temperature range, $T > 2 \times 10^4$ K, the cooling rate for solar metallicity is taken from Sutherland & Dopita (1993). We note that in our calculations the gas temperature is generally below 10^4 K, higher temperature is reached only in small rarefied regions at the periphery of the disc.

The heating rate Γ in the equation (4) takes into account photoelectric heating on the dust particles (Bakes & Tielens 1994; Wolfire et al. 2003), heating due to H_2 formation on the dust and the H_2 photodissociation (Hollenbach & McKee 1979) and the ionization heating by cosmic rays (Goldsmith et al. 1978). The details can be found in Appendix B.

2.4 Numerical methods

To solve the system of gas dynamical equations (1)–(4) we use nonlinear finite-volume numerical scheme total variation diminishing (TVD) Monotone Upstream-centered Schemes for Conservation Laws (MUSCL) in the Cartesian coordinates (van Leer 1979). The continuity equation for chemical species is constructed using the operator splitting scheme. Note that because in our model we have two chemical species, H I and H_2, we can solve the kinetics equation for one of them only, e.g. for H_2. At first we solve the continuity equation without right-hand terms and update the H_2 density due to advection. Than we update this result after solution of chemical reactions. The equation for H_2 (equation 7) is integrated using a fourth-order Runge–Kutta method. To find the gravitational potential of the gas (equation 5) we use the TREECODE method (Barnes & Hut 1986).

The numerical resolution is $4096 \times 4096 \times 20$ cells. The cells are assumed to be cubic with the sides of 7.3 pc. Therefore, the physical size of the computational grid is $30 \times 30 \times 0.15$ kpc. We also made calculations with higher resolution in the vertical direction, but lower in the disc plane direction, e.g. $1024 \times 1024 \times 100$, and did not find significant difference in global characteristics of gas evolution. We expect that this is sufficient to model the large-scale dynamics of the Galactic disc and to study the formation of the spurs and molecular clouds in the vicinity of the spiral arms.

3 DISC EVOLUTION

Fig. 2 shows the surface gas density at 50, 100, 200 and 300 Myr. At the beginning the spiral shocks are formed due to the supersonic gas flow through the spiral gravitational potential of the stellar disc. After $t = 50$ Myr one finds a well-developed spiral structure in the gas disc (upper left-hand panel). The width of the gas spirals is significantly smaller than that of the stellar density wave due to higher stellar velocity dispersion. At this stage strong shear flows are formed behind the shock fronts. This leads to fast development of Kelvin–Helmholtz instability of shock front. Shocks become dynamically unstable, i.e. small-scale ripples grow or, in other words, the shock wiggles. Owing to shear and wiggle instabilities the shock front becomes perturbed, and as a result the spurs and fragments are formed. Such spurs and fragments can be found at $t = 50$ Myr (upper left-hand panel) and are clearly seen at $t = 100$ Myr (upper right-hand panel). On one hand, higher density in such fragments stimulates molecular hydrogen formation and, as a consequence, efficient cooling of gas in the fragments. On the other hand, the cooling can lead to further fragmentation. We find that the efficient molecule formation starts at $t \sim 30$–50 Myr, which corresponds to the time-scale of molecular hydrogen formation on the dust grains. A major part of the H_2 molecules is formed in such fragments, which are the progenitors of molecular clouds. Note that a number of fragments formed may have super-Jeans masses. So, further

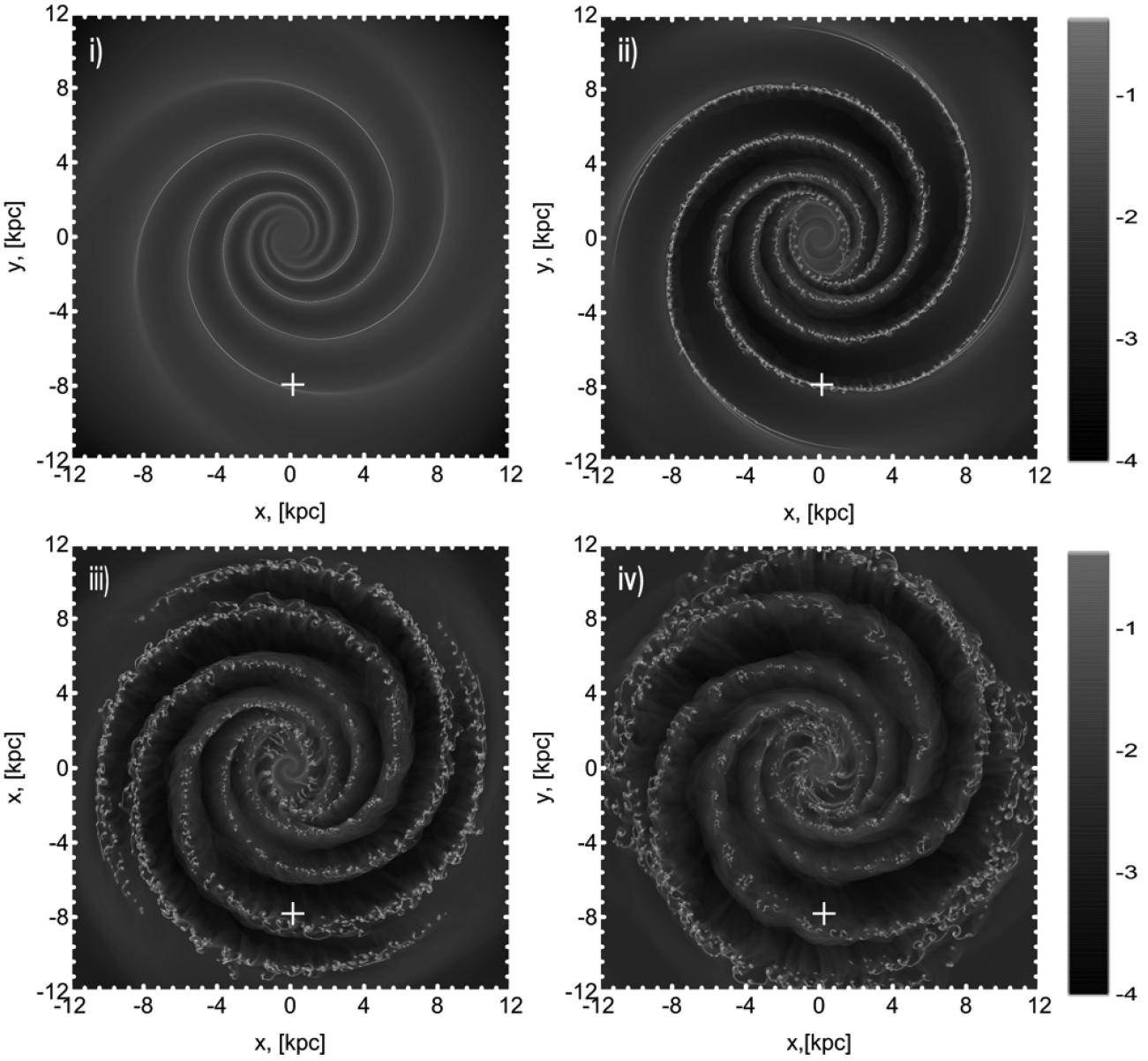

Figure 2. The evolution of the surface density of gas (g cm^{-2}) at $t = 50$ (upper left), 100 (upper right), 200 (lower left) and 300 Myr (lower right). The cross shows position of the Sun (8 kpc).

fragmentation is expected to be amplified by both thermal instability and self-gravity.

A large number of clouds are formed as a result of further evolution: a flocculent structure in the spiral arms can be clearly seen at $t = 200$ Myr (lower left-hand panel of Fig. 2). In the course of collisions the clouds can merge and form bigger ones or can be disrupted completely. In the latter case they produce a number of smaller clouds. The clouds moving supersonically through the interstellar medium can be stripped due to the Kelvin–Helmholtz instability. Though H_2 molecules are formed and destroyed due to these processes, the total mass of molecular gas in the Galaxy increases until $t \sim 200$ Myr. Then it saturates because the quasi-stationary regime is established between the molecule formation on dust and their destruction by the UV radiation from OB stars (lower left-hand panel of Fig. 2). So, at $t \sim 200$ Myr one finds a population of clouds with sizes varying in the range ∼10–100 pc and typical lifetime about 10 Myr (in the next section we analyse the properties of the clouds in more detail).

At $t = 200$ Myr groups of clouds are settled along the spiral arms (Fig. 2). During further evolution these groups become larger both in size and mass. Gradually they stand apart from each other in the spiral arms. Such agglomerations of clouds have sizes more than 100 pc and the distance between such associations at $t = 300$ Myr reaches several hundred parsecs. The agglomerations consist of several clouds with the typical number density $\gtrsim 1$ cm^{-3}. The typical thermal pressure $p_{\rm th}/k_{\rm B}$ within such clouds is about (3–10) $\times$ 10^4 K cm^{-3} which corresponds to the temperatures $T \sim 80$–100 K. Actual values of the gas temperature are lower because considerable portion of the internal energy is spent on the turbulent motions. However numerical resolution of our simulations is not high enough to resolve the inner structure of the molecular clouds and the turbulent flows. The turbulence (especially small-scale one) represents

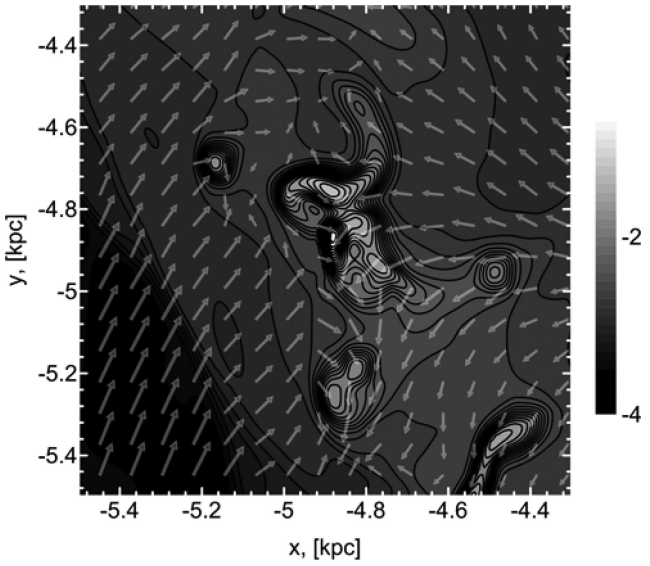

Figure 3. The surface gas density (g cm^{-2}) and the velocity field (in the comoving coordinate system) of the 'cloud' with coordinates (−4.9, −4.9 kpc) at $t = 300$ Myr.

a common and complex problem. At this stage we are not able to extract the turbulent part of the internal energy.

The velocity dispersion in a gas around molecular clouds is about 3–7 km s^{-1} and the velocity field around clouds shows a complex turbulent structure. To consider this we pick out a cloud with coordinates (−4.9, −4.9 kpc) at $t = 300$ Myr. Fig. 3 shows velocity field around such cloud. The velocities are shown in the comoving coordinate system connected to the most dense part of the cloud. One can see the irregular form of the cloud and the colliding gaseous flows in the regions with enhanced density. The structure and physical parameters of the cloud locations obtained in our numerical simulations are close to those observed in the GMCs and their surroundings (Román-Duval et al. 2010).

Thermochemical processes taken into account in our simulations lead to formation of the two phases of the simulated gas with stable points around ∼80 and ∼10^4 K (Fig. 4, see note on the value of the temperature above). A gas with $T \sim 80$ K corresponds to the dense molecular clouds, i.e. they have both high number density ($n \sim$ 100–300 cm^{-3}) and high H_2 molecule abundance ($x(H_2) \sim 0.3$–0.5). These clouds concentrate to the spiral arms. A gas belonging to the warmer phase with $T \sim 10^4$ K is a rarefied atomic gas which resides mainly between the arms.

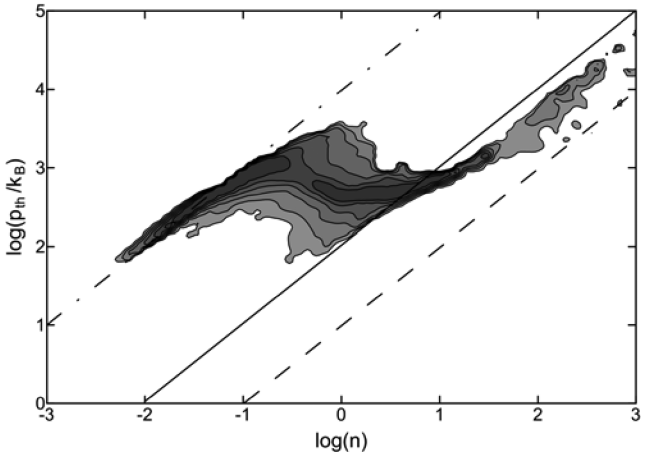

Figure 4. The phase diagram of thermal pressure $p_{\rm th}$ normalized by Boltzman's constant (K cm^{-3}) versus number density of gas n (cm^{-3}) at the time $t = 300$ Myr. The lines correspond to the constant temperature (see note on the value of the temperature in the text): 10 (dashed line), 10^2 (solid line) and 10^4 K (dash–dotted line).

4 THE PHYSICAL PROPERTIES OF MOLECULAR CLOUDS

In this section we consider physical and statistical properties of the molecular gas in our simulations. This gas resides in the clumps which are called molecular clouds. A border of the cloud can be defined as location where H_2 abundance or H_2 surface density exceeds given limit. The clouds in our analysis are delimited using a surface density threshold: over the 2D computational grid of the Galactic plane we find isolated groups of cells with the column density exceeding given threshold. Such clumps normally have irregular form, and their effective linear size is estimated as a square root of their surface.

For our analysis we have chosen two values of the molecular hydrogen surface density threshold: $\Sigma_{\rm t}^{\rm H_2} = 1.5 \times 10^{-5}$ and 1.5×10^{-4} g cm^{-2}. In both cases average density inside a cloud has values about several dozen particles per cubic centimetre, which is close to the typical value of H_2 number density obtained from observations of molecular clouds in the Galaxy (e.g. Shu et al. 1987).

We are using two thresholds for H_2 surface density at the border of the cloud in order to show that our basic conclusions on the statistical properties of clouds are independent of exact value of the threshold. This is important because there is no single value of H_2 surface density which exactly reproduces definition of a molecular cloud in observations.

Fig. 5 presents the distribution of masses of the clouds for the H_2 surface density thresholds $\Sigma_{\rm t}^{\rm H_2} = 1.5 \times 10^{-5}$ (solid line) and 1.5×10^{-4} g cm^{-2} (dash line) at $t = 300$ Myr.

We find that the spectra of cloud masses for both thresholds follow the power-law dependence $N \sim M^{-1.64}$: in the mass range $M \sim 10^5$–10^6 M$_\odot$ for the higher threshold value and in mass range $M \sim 10^6$–10^7 M$_\odot$ for the lower density threshold. This invariance of the spectrum on surface density limit indicates to that physical

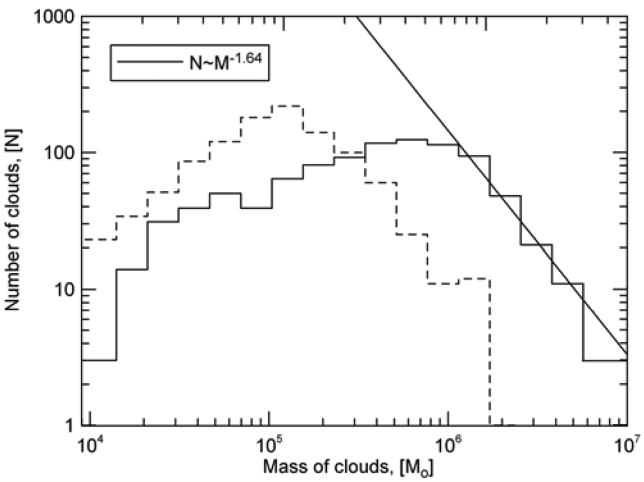

Figure 5. Distribution of masses of the clouds for the H_2 surface density thresholds $\Sigma_{\rm t}^{\rm H_2} = 1.5 \times 10^{-5}$ (solid line) and 1.5×10^{-4} g cm^{-2} (dash line) at $t = 300$ Myr. The line corresponds to the empirical dependence $N \sim M^{-1.64}$ obtained by Román-Duval et al. (2010).

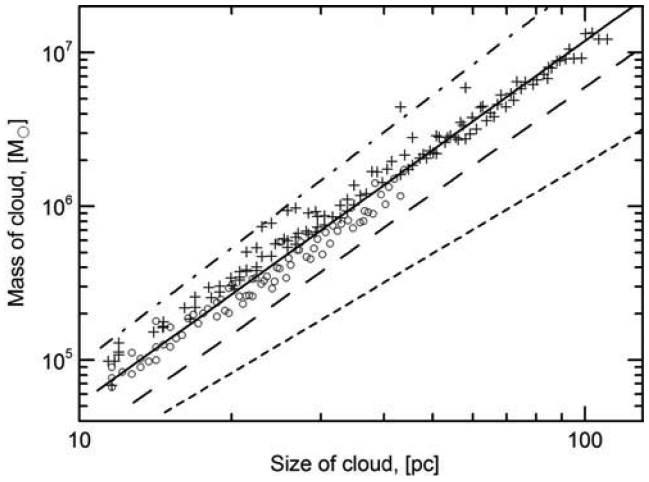

Figure 6. Mass–size dependence for the H_2 surface density thresholds $\Sigma_t^{H_2} = 1.5 \times 10^{-5}$ (crosses) and 1.5×10^{-4} g cm^{-2} (circles) at $t = 300$ Myr. The lines correspond to several theoretical and empirical fits $(M/M_\odot) = \gamma(A/pc^2)^\beta$ given in Beaumont et al. (2012): $(\gamma, \beta) = 240$, 0.95 (Larson 1981), $(\gamma, \beta) = 300$, 1.5 (Elmegreen & Falgarone 1996), $(\gamma, \beta) = 150$, 1.3 (Román-Zúñiga et al. 2010) and $(\gamma, \beta) = 228$, 1.36 (Román-Duval et al. 2010) shown by dotted, dashed, solid and dash–dotted lines, respectively.

processes leading to the formation of the structure with density threshold $\Sigma_t^{H_2} \sim 10^{-5}$–$10^{-4}$ g cm^{-2} have the same nature. Hence, other statistical properties of the structures should be close. Note that the dependence $N(M)$ for the higher threshold is valid in the same mass range as that obtained in the observations of the Galactic molecular clouds (Román-Duval et al. 2010). For both thresholds one can see a lack of low-mass clouds. In the case of the higher limit the lack of clouds with $M \lesssim 10^5\,M_\odot$ can be explained by our numerical resolution, whereas similar deficiency in the observations comes from the incompleteness of the data (Román-Duval et al. 2010). For the lower threshold the lack of clouds with $M \lesssim 10^6\,M_\odot$ can be explained by clustering of smaller and denser clumps. In other words, choosing lower surface density level we pick out more extended clusters of clumps, which contain both smaller and denser clumps. In the case of the lower threshold we cover larger regions with lower density, so that the increase of density limit should lead to decrease of size of the cluster and excludes extended low-density regions from consideration of.

Fig. 6 presents the dependence of mass of the cloud on its size (mass–size relationship) for the H_2 surface density thresholds $\Sigma_t^{H_2} = 1.5 \times 10^{-5}$ (crosses) and 1.5×10^{-4} g cm^{-2} (circles) at $t = 300$ Myr. The sizes of the clouds vary between ∼10 and 60 pc for the higher density threshold. The most massive clouds have masses about $2 \times 10^6\,M_\odot$. These values are in good agreement with the observational data (Román-Duval et al. 2010). In some cases the sizes of molecular clouds can be as large as ∼100–200 pc (Kirsanova et al. 2008) but these regions can be considered as a tight group of smaller clouds. In our analysis such extended clouds can be found under the lower density threshold (crosses in Fig. 6): there are groups or chains of clouds seen in the periphery of the Galaxy at 300 Myr (Fig. 2).

The mass–size (or mass–area) relationship among molecular clouds, $M \sim R^2$, which is well known as Larson's third law, appears due to cloud evolution and numerous physical processes in the interstellar medium. Many efforts to obtain or explain this universal relation are given in Beaumont et al. (2012), who tried to interpret the relationship in terms of the column density distribution function. However, the scatter of the empirical fits is large (see lines in Fig. 6, note that we pick out only several fits from table 1 presented in Beaumont et al. 2012). One can see that the properties of clouds obtained in the numerical simulations are close to the power-law relation between the radius and mass of the cloud $M = 228R^{2.36}$, which was obtained by applying a χ^2 minimization for the observed radii and masses of the Galactic molecular clouds (Román-Duval et al. 2010). There is a significant dispersion of our simulated data around this fit. We find that our best fit of the simulated data $M \sim R^{2.14\text{–}2.16}$ (the ranges correspond different density thresholds) is close to that obtained in observations. Note that our fit has a power-law index close to 2 for both density thresholds considered here.

Finally, we note that the velocity dispersion for the majority of clouds varies in the range $v_t \sim 1$–$2\,\mathrm{km\,s^{-1}}$ in our numerical simulations, that is a good agreement with the observational data (Román-Duval et al. 2010).

Thus, we have found that the physical properties of clouds obtained from our simulation are close to those observed in the Galaxy. Our conclusions are constrained by the numerical resolution, because we can consider clouds with sizes larger than 10 pc, whereas even the parsec-size clouds are observed (Román-Duval et al. 2010). Anyhow, our numerical results provide possibility to consider the global properties of molecular and atomic gas in the Galaxy.

5 THE *l–v* DIAGRAM

5.1 Molecular hydrogen

Large-scale distribution of molecular gas in the Galaxy can be represented using the 'longitude–velocity' diagram (henceforth *l–v* diagram) constricted from observations of the CO(1–0) line emission (Dame et al. 2001). The CO molecule is usually used as a tracer of molecular gas (Maloney & Black 1988) because emission of much more abundant H_2 molecule cannot be observed in the cold and warm regions. Current model of molecular kinetics in our simulations does not provide us with possibility to calculate abundance of CO molecule and the distribution of molecular gas is judged from the distribution of H_2. Certainly, the CO–H_2 conversion factor depends on many physical parameters (Shetty et al. 2011; Feldmann, Gnedin & Kravtsov 2012). However, there are no doubts that the general conclusion on agreement between synthetic and observational distributions of molecular gas in the Galaxy can be drawn from comparison of *l–v* diagram for H_2 molecule in the model with CO data of Dame et al. (2001).

Fig. 7 presents the *l–v* diagram for molecular gas at $t = 300$ Myr. The diagram is constructed for an observer located at the Sun position (see Fig. 2). One can find the large-scale structures corresponding to Perseus, Outer and Carina spiral arms. In the central part of the diagram, $l \pm (30^\circ\text{–}40)^\circ$, an intense and extended structure with the strong velocity gradient that passes through the origin is clearly seen. This structure by its location and general appearance resembles so-called Galactic molecular ring (Stecker et al. 1975; Cohen & Thaddeus 1977; Román-Duval et al. 2010). However, Fig. 2 shows that there is no pronounced ring of molecular material in our simulations. In our model the structure in the molecular ring locus of points of the *l–v* diagram is associated with the Galactic bar and the spiral arms at ∼3–4 kpc. Thus, our results are in agreement with conclusions on the absence of the molecular ring drawn from the simple fitting technique (Dobbs & Burkert 2012) and previous hydrodynamical simulations (Englmaier & Gerhard 1999; Rodriguez-Fernandez & Combes 2008; Baba, Saitoh & Wada

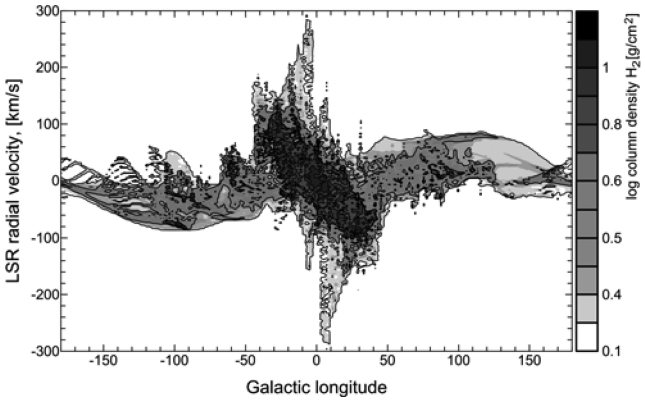

Figure 7. The l–v diagram for the molecular gas at $t = 300$ Myr. The mass of gas with a given (l, v) is indicated by grey-scale: from small (light grey) to large (black) mass.

2010). Note that the previous simulations did not include molecular chemical kinetics.

We have to note on the existence of numerous small-scale structures in the diagram. They are obviously associated with spurs, agglomerations of clouds and individual clouds. But we make no comment on that here because our consideration is concentrated on the extended structures scales of which greatly exceed our numerical resolution.

5.2 Atomic hydrogen

The atomic gas in our model is the main part of the gaseous component of the spiral arms and its distribution traces large-scale structures in the Galaxy. Fig. 8 presents the synthetic l–v diagram for atomic gas at $t = 300$ Myr. The diagram is constructed for an observer located at the Sun position (see Fig. 2). The structures corresponding to the spiral arms are clearly seen in this figure. The synthetic diagram does not show any prominent structure at the locus of points corresponding to the Galactic molecular ring (Fig. 8). Results of our modelling show that the atomic gas in the simulated Galaxy is distributed much more uniformly than the molecular gas. The synthetic l–v diagram shows reasonably good agreement with the observational data (see e.g. l–v diagrams in Mc Clure-Griffiths et al. 2004; Kalberla & Dedes 2008). So, our model reproduces main features of the observed distribution of the neutral gas in the Galaxy.

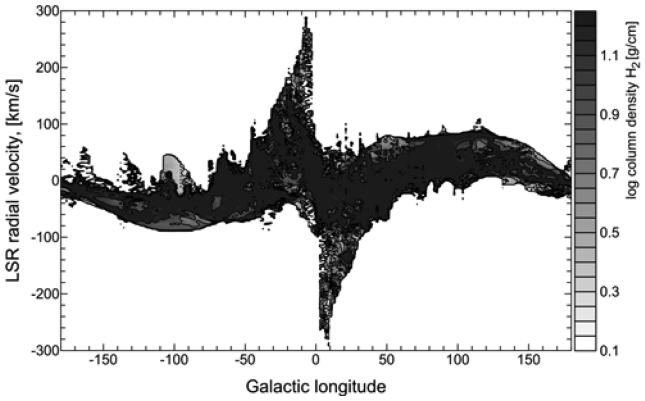

Figure 8. The l–v diagram for the atomic gas at $t = 300$ Myr. The mass of gas with a given (l, v) is indicates by grey-scale: from small (light grey) to large (black) mass.

6 CONCLUSION

In this paper we have studied formation of gas clouds in the model of our Galaxy. The 3D simulations have taken into account molecular hydrogen chemical kinetics, cooling and heating processes. Comprehensive gravitational potential have been used. It included contributions of self-gravitating gaseous component, stellar bulge, two- and four-armed spiral structure, stellar disc and dark halo. We have analysed general properties of the simulated clouds and have compared them with statistical distributions taken from the recent surveys of molecular clouds (Román-Duval et al. 2010).

Our results can be summarized as follows:

(i) the following stages of evolutionary sequence of the molecular cloud system formation were distinguished in our modelling: (a) spurs and fragments (progenitors of molecular clouds) are formed in the spiral arms due to shear and wiggle instabilities at the times $t \lesssim 50$ Myr; (b) numerous molecular clouds start to form after $t \gtrsim 50$ Myr which corresponds to the time-scale of molecular hydrogen formation on dust grains; (c) a well-developed hierarchical structure of the clouds is formed at $t \sim 200$ Myr; (d) at the moment of time $t \sim 300$ Myr the clouds agglomerate into extended associations with sizes exceeding 100 pc while the sizes of individual clouds vary in the range ∼10–100 pc;

(ii) the total mass of molecules in the Galaxy increases until $t \sim 200$ Myr, when it saturates; the major part of molecule hydrogen is locked in molecular clouds where the H_2 molecule abundance reaches $x(H_2) \sim 0.3$–0.5;

(iii) the statistical dependencies, e.g. the mass spectrum of clouds, the 'mass–size' relation and the velocity dispersion of clouds, obtained in our simulations are close to those observed in the Galaxy (Román-Duval et al. 2010);

(iv) the structure is clearly seen in the Galactic molecular ring's locus of points on the simulated l–v diagram of molecular gas; this structure does not correspond to a real ring of molecular gas and likely arises due to superposition of emission from the galactic bar and the spiral arms at ∼3–4 kpc, which supports conclusion made by Dobbs & Burkert (2012); no prominent structure in the Galactic molecular ring locus of points is distinguished in the simulated l–v diagram of the H I gas.

ACKNOWLEDGMENTS

The authors are thankful to A. V. Zasov and Yu. A. Shchekinov for valuable discussions. This work was supported partially by Russian Foundation for Basic Research (grants 11-02-12247, 10-02-00231, 12-02-00685 and 12-02-31452) and the President of the Russian Federation grant (SS-3602.2012.2). SAK and EOV thank foundation 'Dynasty' (Dmitry Zimin) for financial support. EOV and AMS thank Russian Foundation for Basic Research (grants 11- 02-01332 and 11-02-97124-p). AMS was partly supported by the Russian federal task program 'Research and operations on priority directions of development of the science and technology complex of Russia for 2007–2013' (state contract 14.518.11.7064). Numerical simulations were implemented with supercomputer facilities 'Lomonosov' and 'Chebyshev' of the Moscow State University.

REFERENCES

Amores E. B., Lepine J. R. D., Mishurov Yu. N., 2009, MNRAS, 400, 1768
Asplund M., Grevesse N., Sauval A. J., 2005, in Barnes T. G., Bash F. N., eds, ASP Conf. Ser. Vol. 336, Cosmic Abundances as Records of Stellar Evolution and Nucleosynthesis. Astron. Soc. Pac., San Francisco, p. 25

Baba J., Saitoh T. R., Wada K., 2010, PASJ, 62, 1413
Bakes E. L. O., Tielens A. G. G. M., 1994, ApJ, 427, 822
Balbus S. A., Cowie L. L., 1985, ApJ, 297, 61
Ballesteros-Paredes J., Klessen R. S., Mac Low M.-M., Vazquez-Semadeni E., 2007, in Reipurth B., Jewitt D., Keil K., eds, Protostars and Planets V. University of Arizona Press, Tucson, p. 63
Barnes J., Hut P., 1986, Nat, 324, 446
Beaumont C. N., Goodman A. A., Alves J. F., Lombardi M., Román-Zúñiga C. G., Kauffmann J., Lada C. J., 2012, MNRAS, 423, 2579
Begeman K. G., Broeils A. H., Sanders R. H., 1991, MNRAS, 249, 523
Bergin E. A., Hartmann L. W., Raymond J. C., Ballesteros-Paredes J., 2004, ApJ, 612, 921
Binney J., Tremaine S., 2008, Galactic Dynamics, 2nd edn. Princeton Univ. Press, Princeton, NJ
Blitz L., Shu F. H., 1980, ApJ, 238, 148
Bobylev V. V., Bajkova A. T., 2010, MNRAS, 408, 1788
Cazaux S., Tielens A. G. G. M., 2004, ApJ, 604, 222
Cen R., 1992, ApJS, 78, 341
Chou W., Matsumoto R., Tajima T., Umekawa M., Shibata K., 2000, ApJ, 538, 710
Cohen R. S., Thaddeus P., 1977, ApJ, 217, L155
Cox D. P., Gomez G. C., 2002, ApJS, 142, 261
Dame T. M., Elmegreen B. G., Cohen R. S., Thaddeus P., 1986, ApJ, 305, 892
Dame T., Hartmann D., Thaddeus P., 2001, ApJ, 547, 729
Dobbs C. L., 2008, MNRAS, 391, 844
Dobbs C. L., Bonnell I. A., 2006, MNRAS, 367, 873
Dobbs C. L., Bonnell I. A., 2007a, MNRAS, 374, 1115
Dobbs C. L., Bonnell I. A., 2007b, MNRAS, 376, 1747
Dobbs C. L., Burkert A., 2012, MNRAS, 421, 2940
Dobbs C. L., Bonnell I. A., Pringle J. E., 2006, MNRAS, 371, 1663
Draine B. T., Bertoldi F., 1996, ApJ, 468, 269
Elmegreen B. G., 1979, ApJ, 231, 372
Elmegreen B. G., 1994, ApJ, 433, 39
Elmegreen B., Falgarone E., 1996, ApJ, 471, 816
Englmaier P., Gerhard O., 1999, MNRAS, 304, 512
Falgarone E., Puget J.-L., Perault M., 1992, A&A, 257, 715
Feldmann R., Gnedin N. Y., Kravtsov A. V., 2012, ApJ, 747, 124
Field G. B., Saslaw W. C., 1965, ApJ, 142, 568
Fridman A. M., Khoperskov A. V., 2011, Physics of Galactic Disks. Fizmatlit, Moscow (in Russian)
Galli D., Palla F., 1998, A&A, 335, 403
Glover S. C. O., Mac Low M., 2011, MNRAS, 412, 337
Goldsmith P., Langer W. D., 1978, ApJ, 222, 881
Habing H. J., 1968, Bull. Astron. Inst. Netherlands, 19, 421
Heyer M., Krawczyk C., Duval J., Jackson J. M., 2009, ApJ, 699, 1092
Hollenbach D., McKee C. F., 1979, ApJS, 41, 555
Hollenbach D., McKee C. F., 1989, ApJ, 342, 306
Kalberla P. M. W., Dedes L., 2008, A&A, 487, 951
Kauffmann J., Pillai T., Shetty R., Myers P. C., Goodman A. A., 2010, ApJ, 712, 1137
Khoperskov A. V., Tyurina N. V., 2003, Astron. Rep., 47, 443
Khoperskov S. A., Khoperskov A. V., Eremin M. A., Butenko M. A., 2011, Astron. Lett., 37, 563
Kim W.-T., Ostriker E. C., 2006, ApJ, 646, 213
Kirsanova M. S., Sobolev A. M., Thomasson M., Wiebe D. S., Johansson L. E. B., Seleznev A. F., 2008, MNRAS, 388, 729
Kwan J., Valdes F., 1987, ApJ, 315, 92
Lada C. J., Lada E. A., 2003, ARA&A, 41, 57
Lada C. J., Muench A. A., Rathborne J., Alves J. F., Lombardi M., 2008, ApJ, 672, 410
Larson R. B., 1981, MNRAS, 194, 809
Lepine J. R. D., Mishurov Yu. N., Dedikov S. Yu., 2001, ApJ, 546, 234
Levine E. S., Blitz L., Heiles C., 2006, Sci, 312, 1773
Levinson F. H., Roberts W. W., Jr, 1981, ApJ, 245, 465
McClure-Griffiths N. M., Dickey J. M., Gaensler B. M., Green A. J., 2004, ApJ, 607, L127
McKee C. F., Ostriker E. C., 2007, ARA&A, 45, 565
Mac Low M.-M., Shull J. M., 1986, ApJ, 302, 585
Maloney P., Black J. H., 1988, ApJ, 325, 389
Mishurov I. N., Suchkov A. A., 1975, Ap&SS, 35, 285
Nelson A. H., Matsuda T., 1977, MNRAS, 179, 663
Rathborne J. M., Johnson A. M., Jackson J. M., Shah R. Y., Simon R., 2009, ApJS, 182, 131
Roberts W. W., 1969, ApJ, 158, 123
Roberts W. W., Stewart G. R., 1987, ApJ, 314, 10
Rodriguez-Fernandez N. J., Combes F., 2008, A&A, 489, 115
Román-Duval J., Jackson J. M., Heyer M., Rathborne J., Simon R., 2010, ApJ, 723, 492
Román-Zúñiga C. G., Alves J. F., Lada C. J., Lombardi M., 2010, ApJ, 725, 2232
Shetty R., Ostriker E. C., 2006, ApJ, 647, 997
Shetty R., Glover S. C., Dullemond C. P., Ostriker E. C., Harris A. I., Klessen R. S., 2011, MNRAS, 415, 3253
Shu F. H., Adams F. C., Lizano S., 1987, ARA&A, 25, 23
Sofue Y., Honma M., Omodaka T., 2009, PASJ, 61, 227
Solomon P. M., Rivolo A. R., Barrett J., Yahil A., 1987, ApJ, 319, 730
Stecker F. W., Solomon P. M., Scoville N. Z., Ryter C. E., 1975, ApJ, 201, 90
Sutherland R. S., Dopita M. A., 1993, ApJS, 88, 253
Tasker E. J., Tan J. C., 2009, ApJ, 700, 358
Tielens A. G. G. M., Hollenbach D., 1985, ApJ, 291, 722
Tomisaka K., 1984, PASJ, 36, 457
Vallee J. P., 2005, AJ, 130, 569
van Leer B., 1979, J. Comput. Phys., 32, 101
Wada K., 1994, PASJ, 46, 165
Wada K., 2001, ApJ, 559, L41
Wada K., Koda J., 2004, MNRAS, 349, 270
Wada K., Spaans M., Kim S., 2000, ApJ, 540, 797
Wolfire M. G., McKee C. F., Hollenbach D., Tielens A. G. G. M., 2003, ApJ, 587, 278
Zhang T. J., Song G. X., 1999, Ap&SS, 266, 521

APPENDIX A: EXTERNAL GRAVITATIONAL POTENTIAL MODEL

The dark matter halo gravitational potential is taken in the quasi-isothermal form (Begeman, Broeils & Sanders 1991):

$$\Psi_{\rm halo} = \frac{M_{\rm h}}{C_{\rm h}} \left\{ \ln(\xi) + \frac{\mathrm{arctg}(\xi)}{\xi} + \frac{1}{2} \ln \frac{1+\xi^2}{\xi^2} \right\}, \quad \text{(A1)}$$

where $\xi = r/a_{\rm h}$, $M_{\rm h}$ is the mass of the dark halo within a radius $r_{\rm h}$, $a_{\rm h}$ is the scale of the halo and $C_{\rm h} = a_{\rm h}(r_{\rm h}/a_{\rm h} - \mathrm{arctg}(r_{\rm h}/a_{\rm h}))$. In our model we take $r_{\rm h} = 12$ kpc, $a_{\rm h} = 6$ kpc and $M_{\rm h} = 0.64 \times 10^{11}\,{\rm M}_\odot$.

For the stellar bulge potential we adopt the King's model with the cut-off at radius $r_{\rm b}^{\rm max}$ (Fridman & Khoperskov 2011):

$$\Psi_{\rm bulge} = -\frac{M_{\rm b}}{r C_{\rm b}} \ln \left[\frac{r}{r_{\rm b}} + \left(1 + \left(\frac{r}{r_{\rm b}} \right)^2 \right) \right], \quad \text{(A2)}$$

with the following parameters $M_{\rm b} = 0.092 \times 10^{11}\,{\rm M}_\odot$, $r_{\rm b} = 0.2$ kpc, $r_{\rm b}^{\rm max} = 12$ kpc, where

$$C_{\rm b} = \ln \left(r_{\rm b}^{\rm max}/r_{\rm b} + \sqrt{1 + (r_{\rm b}^{\rm max}/r_{\rm b})^2} \right) - \left(r_{\rm b}^{\rm max}/r_{\rm b} \right) / \left(\sqrt{1 + (r_{\rm b}^{\rm max}/r_{\rm b})^2} \right).$$

For the three-dimensional stellar disc we take the exponential distribution of surface density, then the stellar disc potential can be written as follows (Binney & Tremaine 2008):

$$\Psi_{\rm disc} = \pi \sigma_0 z_{\rm d} \ln(\cosh(z/z_{\rm d})) - \pi \sigma_0 r_{\rm d}\, y\, (I_0(y) K_1(y) - I_1(y) K_0(y)), \quad \text{(A3)}$$

where $y = \frac{r}{2r_d}$, $\sigma_0 = \frac{M_d}{2\pi r_d^2}$ is the central surface density, $M_d = 0.4 \times 10^{11}\,M_\odot$, the radial scale of disc $r_d = 3$ kpc, the vertical scale $z_d = 100$ pc, $I_0(y)$, $K_0(y)$, $I_1(y)$, $K_1(y)$ are the cylindrical Bessel functions of the first and second kind, respectively.

Taking account the gravitational potentials of bar and spiral structure of stellar component we can obtain more realistic distribution of gas in the Galaxy. Following Cox & Gomez (2002) the perturbed potential of stellar disc $\Psi^*_{\rm disc}$ can be written in the form of superposition of potentials generated by the bar and the two- and four-armed logarithmic spiral patterns:

$$\Psi^*_{\rm disc} = \Psi_{\rm disc}(1 + \varepsilon(t)\Psi_{\rm arms}), \tag{A4}$$

where $\varepsilon(t)$ describes the evolution of the relative amplitude of the spiral stellar density wave. We assume a linear increase of the amplitude $\varepsilon(t < \tau) = 0.1\,t/\tau$ during $\tau = 220$ Myr, after that time the amplitude is constant: $\varepsilon(t > \tau) = 0.1$.

The relative perturbation $\Psi_{\rm arms}$ is adopted in the form (Wada & Koda 2004):

$$\Psi_{\rm arms} = \frac{\kappa_1 \cos(\Theta_1)}{(1+\kappa_1)^{3/2}} + \frac{\kappa_2 \cos(\Theta_2)}{(1+\kappa_2)^{3/2}} + \frac{\kappa_4 \cos(\Theta_4)}{(1+\kappa_4)^{3/2}}, \tag{A5}$$

where $\kappa_1 = (r/r_{a1})^2$, $\kappa_2 = (r/r_{a2})^2$, $\kappa_4 = (r/r_{a4})^2$; $r_{a1} = 2$ kpc, $r_{a2} = 7$ kpc and $r_{a4} = 7$ kpc are the radial scales for bar, two-armed and four-armed spiral patterns, respectively. The functions Θ_i are

$$\Theta_1 = 2(\varphi - f_1),$$

$$\Theta_2 = 2\,(\varphi - f_2 - \cot(i_2)\ln(r/r_{02}))\,,$$

$$\Theta_4 = 4\,(\varphi - f_4 - \cot(i_4)\ln(r/r_{04}))\,,$$

where φ is the azimuthal angle, $f_1 = f_2 = f_4 = 50^\circ$ are the azimuthal phases of bar and spiral patterns, $r_{02} = r_{04} = 3.5$ kpc, $i_2 = i_4 = 18^\circ$ are the scales and the pitch angles of two-armed and four-armed components, respectively.

APPENDIX B: COOLING AND HEATING RATES

In this section we present the list of cooling and heating rates for the low temperature range, $T < 2 \times 10^4$ K. The main cooling processes for the solar-metallicity gas are the hydrogen recombination and excitation in the range of temperatures $10^4 \lesssim T \lesssim 2 \times 10^4$ K, and emission in the fine-structure lines of C II, O I and Si II when the temperature is $T \lesssim 10^4$ K. The atomic data for the fine-structure transitions are adopted from Hollenbach & McKee (1989) and presented in Table B1. The cooling rates in the lines are obtained by solving the equation for the level populations in the optically thin steady-state regime (see e.g. Hollenbach & McKee 1979). In Table B2 we summarize other thermal processes which are influential for the cooling and heating of the gas. In Table B1 we adopt the following notation: λ is the line wavelength, $E_{ij}/k_{\rm B}$ is the excitation temperature, A_{ij} is the Einstein coefficient, $\gamma^{\rm e}_{ij}$, $\gamma^{\rm H}_{ij}$ are de-excitation rates due to collisions with electrons and atomic hydrogen, respectively. In Table B2 we assume the following notation: n is the gas number density, Z is the gas metallicity, $n_{\rm H}$, $n_{\rm H_2}$, $n_{\rm e}$, $n_{\rm H^+}$ ($n_{\rm e} = n_{\rm H^+}$), $n_{\rm O\,I}$, $n_{\rm C\,II}$, $n_{\rm Si\,II}$ are neutral hydrogen, molecular hydrogen, electron and proton, neutral oxygen, singly ionized carbon, singly ionized silicon number densities, respectively; temperature of dust grains is assumed to be equal to $T_{\rm d} = 8$ K; Doppler broadening parameter is assumed to be equal to $b = 3$ km s^{-1}; G_0 denotes density of energy for incident ultraviolet radiation in the range 6–13.6 eV normalized by the Habing (1968) estimate of the local interstellar value ($=1.6 \times 10^{-3}$ erg cm^{-2} s^{-1}); $k^{\rm form}_{\rm H_2}$ is the reaction rate of H_2 formation on dust grains. $\Lambda^{\rm LTE}_{\rm H_2}$ is cooling function under assumption of the local thermal equilibrium (LTE), which is adopted in the form given by Hollenbach & McKee (1979).

Table B1. Atomic data for the fine-structure transitions.

Coolant	Transition	λ (μm)	$E_{ij}/k_{\rm B}$ (K)	A_{ij} (s^{-1})	$\gamma^{\rm e}_{ij}$ (cm^3 s^{-1})	$\gamma^{\rm H}_{ij}$ (cm^3 s^{-1})
C II ($^2P_{1/2}$,$^2P_{3/2}$)	1→0	157.7	91.2	2.4×10^{-6}	$2.8 \times 10^{-7}(T/100)^{-0.5}$	$8.0 \times 10^{-10}(T/100)^{0.07}$
O I ($^2P_2$,$^2P_1$,$^2P_0$)	1→0	63.1	227.7	9.0×10^{-5}	1.4×10^{-8}	$9.2 \times 10^{-11}(T/100)^{0.67}$
	2→0	44.2	326.7	1.0×10^{-10}	1.4×10^{-8}	$4.3 \times 10^{-11}(T/100)^{0.8}$
	2→1	145.6	98	1.7×10^{-5}	5.0×10^{-9}	$1.1 \times 10^{-10}(T/100)^{0.44}$
Si II ($^2P_{1/2}$,$^2P_{3/2}$)	1→0	34.8	410	2.1×10^{-4}	$1.7 \times 10^{-6}(T/100)^{-0.5}$	$8.0 \times 10^{-10}(T/100)^{-0.07}$

Table B2. List of cooling and heating rates.

Process	Rate (erg cm^{-3} s^{-1})	Ref
	Cooling	
H^+ recombination	$\Lambda = 8.7\times10^{-27}T^{0.5}\left(\frac{T}{10^3}\right)^{-0.2} n_e n_{H^+}\left[1+\left(\frac{T}{10^6}\right)^{0.7}\right]^{-1}$	1
H excitation	$\Lambda = 7.5\times10^{-19}\exp\left(-\frac{118\,348}{T}\right) n_e n_H\left[1.0+\left(\frac{T}{10^5}\right)^{0.5}\right]^{-1}$	1
Free–free emission	$\Lambda = 1.42\times10^{-27}T^{0.5}g_{ff}(T)n_e n_{H^+}, \quad g_{ff} = 0.794\,64 + 0.1243\log(T)$	1
H_2 cooling	$\Lambda_{H_2} = \frac{\Lambda_{H_2}^{LTE}}{1+[\Lambda_{H_2}^{LTE}/\Lambda(n_H\to0)]} n_H n_{H_2},$	2
	$\Lambda(n_H\to0) = \log(-103+97.59\log T - 48.05\log T^2 + 10.80\log T^3 - 0.9032\log T^4)$	3
Main metastable transitions	$\Lambda(O\,I\,6300\,Å) = 1.4\times10^{-22}T^{0.5}\exp(-22\,500/T)n_e n_{O\,I}$ $\Lambda(C\,II\,2326\,Å) = 1.22\times10^{-17}T^{0.5}\exp(-61900/T)n_e n_{C\,II}$	4
Gas-dust particles energy transfer	$\Lambda = 3.8\times10^{-33}T^{0.5}(T-T_d)\left[1.0-0.8\exp\left(-\frac{75}{T}\right)\right]\left(\frac{Z}{Z_\odot}\right)n^2$	3
Dust particle surface recombination	$\Lambda = 2.33\times10^{-30}T^{0.94}\tilde{\psi}^{0.74/T^{0.068}}\left(\frac{Z}{Z_\odot}\right)n_e n$, where $\tilde{\psi} = G_0\sqrt{T}/0.5n_e$	5
	Heating	
Photoelectric effect	$\Gamma = 1.3\times10^{-24}\epsilon G_0\left(\frac{Z}{Z_\odot}\right)n$ $\epsilon = \frac{4.9\times10^{-2}}{1.0+4.0\times10^{-3}\tilde{\psi}^{0.73}} + \frac{3.7\times10^{-2}(T/10000)^{0.7}}{1.0+2.0\times10^{-4}\tilde{\psi}}$	5, 6
H_2 formation on the dust	$\Gamma = 7.16\times10^{-12}k_{H_2}^{form}\,n\,n_H\left(\frac{n}{n+n_{cr}}\right)$ $n_{cr} = \frac{10^6T^{-0.5}}{1.6(n_H/n)\exp\left(-\frac{400}{T}\right)^2} + 1.4(n_{H_2}/n)\exp\left(-\frac{12\,000}{T+1200}\right)$	3
	$k_{H_2}^{form} = 3\times10^{-18}T^{0.5}\left[1+0.04(T+T_d)^{0.5}+2\times10^{-3}T+8\times10^{-6}T^2\right]^{-1}$ $\times\,[1+10^4\exp(-600/T_d)]^{-1}$ cm^3 s^{-1}	3
H_2 photodissociation and UV pumping	$\Gamma = \zeta_{diss}(N(H_2), A_V)n_{H_2}\left[6.4\times10^{-13}+2.7\times10^{-11}\left(\frac{n}{n+n_{cr}}\right)\right]$	3
	see equation (8) for $\zeta_{diss}(NH_2, A_V)$	
	$f_{shield}(N(H_2)) = \frac{0.965}{(1+x/b_5)^2} + \frac{0.035}{(1+x)^{0.5}}\exp\left[-8.5\times10^{-4}(1+x)^{1/2}\right],$	7
	$x = N_{H_2}/5\times10^{14}$ cm^{-2}, $b_5 = b/10^5$ cm s^{-1}	
Cosmic ray ionization	$\Gamma = 3.2\times10^{-11}\xi_{tot}n$, where $\xi_{tot} = (\xi_H n_H + \xi_{H_2}n_{H_2})/n$, $\zeta_H = 6\times10^{-18}$ s^{-1}, $\zeta_{H_2} = 2\zeta_H$	8

References: 1 – Cen (1992); 2 – Galli & Palla (1998); 3 – Hollenbach & McKee (1979); 4 – Hollenbach & McKee (1989); 5 – Wolfire et al. (2003); 6 – Bakes & Tielens (1994); 7 – Draine & Bertoldi (1996); 8 – Goldsmith et al. (1978).

This paper has been typeset from a TEX/LATEX file prepared by the author.